International Journal of Fracture **76:** 97–120, 1996.
© 1996 *Kluwer Academic Publishers. Printed in the Netherlands.*

An energy method for calculating the stress intensities in orthotropic bimaterial fracture

PANOS G. CHARALAMBIDES and WENBIN ZHANG
Department of Mechanical Engineering, University of Maryland, Baltimore County, Baltimore, MD 21228-5398, USA

Received 1 January 1995; accepted 30 June 1995

Abstract. An energy based numerical method has been developed for extracting stress intensities at the tip of an interface crack bounded by two orthogonal dissimilar materials and subjected to a general state of stress. The method is most suitable for mixed mode delamination fracture studies often observed in brittle matrix composite laminates. After obtaining the near-tip finite element solution for a given laminated geometry, the elastic energy release rate, i.e., J is computed via the stiffness derivative method. The individual orthotropic stress intensities, K_{I}^{*}, K_{II}^{*} are then calculated at a minimum computational expense from further J calculations perturbed by reciprocal stress intensity increments. Results obtained using the Crack Surface Displacement (CSD) method were found to be in good agreement with those obtained using the energy method. Comparisons with theoretical solutions indicate that the energy method can be used accurately even when relatively coarse finite element meshes containing approximately 200 eight noded isoparametric elements are used. The method provides an effective and reliable tool for studying via the method of finite elements delamination phenomena in composite anisotropic laminates.

1. Introduction

Fracture of bimaterial interfaces has received renewed interest in recent years, primarily driven by our needs to understand and predict macroscopic composite material response to applied mechanical and environmental loadings. For isotropic bimaterial fracture, several numerical methods [1, 2] have been developed to evaluate the individual mode I, II and mode III crack tip stress intensity factors. Primarily two of the above methods are often used to study the near-tip mechanics associated with bimaterial interface cracks. The simplest one relies exclusively on the crack surface displacements predicted via the method of finite elements and is known as the Crack Surface Displacement (CSD) method. The second method uses an energy approach in calculating the mode I and mode II stress intensities for a given geometry. As such, the energy method involves J-integral calculations [1, 3] using the near-tip finite element solutions as well as virtual displacement solutions associated with the near-tip asymptotic boundary value problem. In previous bimaterial fracture studies by Matos, McMeeking, Charalambides and Drory [1], the energy method proved to be extremely efficient and accurate even when relatively coarse meshes were used. In this paper, it is our intent to expand the energy method developed in [1] in order to account for the material orthotropies associated with the fiber-reinforced plies used in composite laminates.

1.1. Near-tip elastic fields

For cracks in homogeneous elastic isotropic systems, the stress and strain fields in the crack tip region are $r^{-(1/2)}$ singular for all three modes of fracture [4], i.e., mode I, which causes only a relative opening mode, mode II or in-plane shearing mode and mode III or out-plane

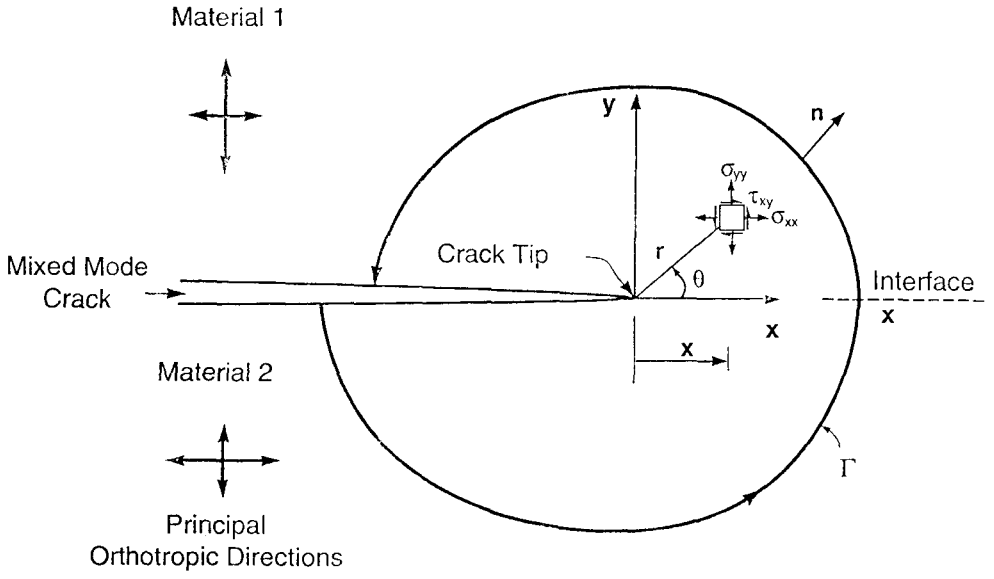

Figure 1. The coordinate system and a typical contour used in the evaluation of the J-integral, for an interface crack bounded by orthotropic dissimilar materials.

shearing mode. It follows that the stress components at a distance r from the crack tip and an angle θ measured as shown in Figure 1 are given in terms of $r^{-(1/2)}$, and a set of universal spatial functions that depend only on θ and the associated components of the stress intensity factor K_{I} for mode I, K_{II} for mode II and K_{III} for mode III. The latter stress intensities can be obtained by and large from the applied loads and from the geometry of the system. Moreover, the nature of the asymptotic solution is such that a nonzero finite energy release rate $\mathcal{G}$ exists at the crack tip and can be obtained from the components of the stress intensity factor and material properties via the generalized Irwin's relationship [4]. In the absence of out-of-plane loading, i.e., $K_{\mathrm{III}} = 0$, it is often convenient to represent the tip stress and strain fields in terms of the energy release rate $\mathcal{G}$ and the associated phase angle Ψ of the complex stress intensity factor $K = K_{\mathrm{I}} + iK_{\mathrm{II}} = |K|e^{i\Psi}$.

Like the singular homogeneous fields, the fields dominating the near-tip region of interface cracks bounded by two dissimilar materials are also $r^{-(1/2)}$ singular and are also parametrized through a complex stress intensity factor $K^* = K_{\mathrm{I}}^* + iK_{\mathrm{II}}^*$. It is important to note that in bimaterial fracture the factors K_{I}^* and K_{II}^* do not in general represent opening and shear fracture modes respectively. In addition, and as discussed by Williams [5] for isotropic bimaterial fracture fields and by others [6–8] for anisotropic bimaterials, the near-tip stress and deformation fields exhibit an oscillatory behavior with respect to the distance from the crack tip. The amplitude and frequency of these oscillations were found to depend on the degree of material mismatch as measured through Dundur's parameters [9] α and β and bimaterial constant ε as well as the degree of anisotropy mismatch through Suo's variables λ and ρ [6]. As discussed elsewhere [5, 6], the in-plane deformations are coupled and oscillatory, and they normalize with the mode I and mode II complex stress intensity factors. The mode III fields exhibit a square root singularity and are dominated by a real stress intensity factor. Recent advances in the field of interfacial fracture are presented in the articles by Rice [10], Suo [6] and Hutchinson [11].

In light of the above, the importance of adopting the pair $\mathcal{G}, \Psi$ as the near-tip characterizing parameters is that $\mathcal{G}$ is a measure of the elastic energy flux to the crack tip due to the application of external loads whereas Ψ, defined as $\Psi = \arctan\left(\frac{K_{II}^*}{K_I^*}\right)$, at least for homogeneous systems is a measure of the relative in-plane sliding and opening of the crack surfaces. In this last relationship, $|K^*|$ represents the modulus of the complex K^* and is uniquely related to $\mathcal{G}$ via the material properties. Thus, in order to fully characterize the stress-strain near-tip fields, one must describe the energy release rate $\mathcal{G}$ and the associated phase angle Ψ in terms of the applied loads and geometry of the system. These quantities can then be used to assess crack growth conditions as elaborated later in this work.

The aim of this paper is to provide a numerical method which can be used reliably to extract from a known finite element solution the stress intensities K_I^* and K_{II}^* dominating the stress and deformation fields in the tip region of an interface crack bounded by two specially orthotropic materials. This work is an extension of that in [1] used for studying the mechanics of fracture between two homogeneous isotropic elastic dissimilar layers.

1.2. Orthotropic bimaterial fracture fields

The mechanics at the tip of an interface planar crack bounded on either side by linear elastic anisotropic layers has been recently studied by Suo [6] and Qu and Bassani [12]. Although, the fundamental salient features of the anisotropic bimaterial near-tip fields have been established through the works of Suo [5] and Qu and Bassani [12], explicit full field solutions for either the displacement or stress field have not yet been reported.

In this study, explicit solutions for both the displacement and stress fields which are valid for the entire near-tip singular domain including the crack surfaces will be developed for the first time. These solutions will then be used in the development of the energy method discussed earlier in this work. With that in mind, we shall address the special case wherein two orthotropic layers are considered on either side of the interface with one of their principal material directions aligned with the crack plane as shown in Figure 1.

For planar, plane stress or plane strain conditions, it has been shown by Lekhniskii [13] and Eshelly et al. [14] that the governing equation for the orthotropic elasticity boundary value problem can be expressed in terms of a stress function $F(x, y)$ in the form of a fourth order partial differential equation as follows

$$S_{22}\frac{\partial^4 F}{\partial x^4} - 2S_{26}\frac{\partial^4 F}{\partial x^3 \partial y} + (2S_{12} + S_{66})\frac{\partial^4 F}{\partial x^2 \partial^2}$$

$$-2S_{16}\frac{\partial^4 F}{\partial x \partial y^3} + S_{11}\frac{\partial^4 F}{\partial y^4} = 0, \tag{1}$$

where S_{ij} are compliances relating the strains ϵ_i to stresses σ_j via the generalized Hook's law as follows

$$\epsilon_i = S_{ij}\sigma_j \qquad (i, j = 1, 6). \tag{2}$$

For generally anisotropic elastic materials the indices i and j vary from 1 to 6 while the transpose of the strain and stress vectors are $\{\epsilon\}^T = \{\epsilon_x, \epsilon_y, \epsilon_z, \gamma_{yz}, \gamma_{zx}, \gamma_{xy}\}$ and $\{\sigma\}^T = \{\sigma_x, \sigma_y, \sigma_z, \tau_{yz}, \tau_{zx}, \tau_{xy}\}$ where the equivalence $x \equiv 1, y \equiv 2, z \equiv 3$ has been assumed.

In particular, for an orthotropic material oriented along its principal axis as shown in Figure 1 under plane stress condition, uncoupling between tension and shear is obtained, such that

$$\begin{aligned} S_{16} &= S_{26} = 0, \\ S_{11} &= \frac{1}{E_1}, \\ S_{12} &= S_{21} = -\frac{\nu_{12}}{E_1} = -\frac{\nu_{21}}{E_2}, \\ S_{22} &= \frac{1}{E_2}, \\ S_{66} &= \frac{1}{G_{12}}, \end{aligned} \tag{3}$$

where $E_i, i = 1, 2, 3$ are the elastic moduli in the principal 1, 2 and 3 directions, respectively; G_{12} is the shear moduli in the 1-2 plane. The Poisson's ratio ν_{23}, ν_{13} and ν_{12} are defined such that $\nu_{ij} = -\frac{\epsilon_j}{\epsilon_i}$ due to an applied normal stress σ_i.

For a ply in plane strain conditions the modified plane strain compliances can be obtained as follows

$$S'_{ij} = S_{ij} - \frac{S_{i3}S_{j3}}{S_{33}} \qquad (i, j = 1, 2), \tag{4}$$

where the non-zero compliances S_{i3} or S_{j3} are given by $S_{13} = \frac{\nu_{31}}{E_1}$, $S_{23} = -\frac{\nu_{32}}{E_2}$ and $S_{33} = \frac{1}{E_3}$.

Thus, for orthotropic planar problems, (1) can be rewritten with the aid of the above equations as follows

$$S_{22}\frac{\partial^4 F}{\partial x^4} + (2S_{12} + S_{66})\frac{\partial^4 F}{\partial x^2 \partial y^2} + S_{11}\frac{\partial^4 F}{\partial y^4} = 0. \tag{5}$$

Suo [6, 7] further simplified the above equation by introducing two non-dimensional orthotropy constants, i.e.,

$$\lambda = \frac{S_{11}}{S_{22}} \quad \text{and} \quad \rho = \tfrac{1}{2}(2S_{12} + S_{66})(S_{11}S_{22})^{-(1/2)},$$

such that when used, (5) takes the form

$$\frac{\partial^4 F}{\partial x^4} + 2\rho\lambda^{1/2}\frac{\partial^4 F}{\partial x^2 \partial y^2} + \lambda\frac{\partial^4 F}{\partial y^4} = 0. \tag{6}$$

A general expression of the stress function $F(x, y)$ was obtained in [13] and has the following form

$$F = 2\mathrm{Re}\,[F_1(Z_1) + F_2(Z_2)], \tag{7}$$

where $F_1(Z_1)$ and $F_2(Z_2)$ are arbitrary complex analytic functions of the complex variables $Z_1 = x + \mu_1 y$ and $Z_2 = x + \mu_2 y$, respectively. The constants, μ_1 and μ_2 are distinct complex numbers with positive imaginary parts and they can be obtained by solving the characteristic equation resulting from (6).

If two new functions are introduced, i.e.,

$$f_1(Z_1) = F_1'(Z_1),$$

$$f_2(Z_2) = F_2'(Z_2),$$

the displacements u_i $(i = 1, 2)$, stresses σ_{ij} $(i = 1, 2)$ and resultant forces T_i $(i = 1, 2)$ acting on an arc Γ are obtained as follows

$$\begin{aligned}
u_i &= 2\mathrm{Re}\left[\sum_{j=1}^{2} \mathbf{A}_{ij} f_j(Z_j)\right] = 2\mathrm{Re}(\mathbf{Af}),\\
\sigma_{1i} &= -2\mathrm{Re}\left[\sum_{j=1}^{2} L_{ij}\mu_j f_j'(Z_j)\right],\\
\sigma_{2i} &= 2\mathrm{Re}\left[\sum_{j=1}^{2} L_{ij} f_j'(Z_j)\right] = 2\mathrm{Re}(\mathbf{Lf}'),\\
T_i &= -2\mathrm{Re}\left[\sum_{j=1}^{2} L_{ij} f_j(Z_j)\right] = -2\mathrm{Re}(\mathbf{Lf}),
\end{aligned} \tag{8}$$

where $()'$ is designated as the derivative with respect to the associated arguments, **A** and **L** are two 2×2 matrices which depend on the elastic constants as listed in Suo's paper [6] and the vector $\mathbf{f} = \{f_1(Z_1), f_2(Z_2)\}^T$.

It has been proven [13,15] that the functions $f_1(Z_1), f_2(Z_2)$ are analytic in the domain defined by $Z = x + \mu y$ with $\mathrm{Im}(\mu) > 0$. For the asymptotic near-tip interface crack problem they lead to an algebraic eigenvalue procedure induced by the boundary conditions. Suo [6] and other researchers [12, 16–19] derived analytical expressions for the stresses and the displacements on the interface crack surface for some fracture problems. More specifically, for the problem shown in Figure 1, the results can be listed as follows.

The stresses ahead of the crack tip are given by

$$\sqrt{\frac{H_{11}}{H_{22}}}\sigma_{yy} + i\sigma_{xy} = (2\pi r)^{-(1/2)} K^* r^{i\varepsilon}, \tag{9}$$

where H_{11}, H_{22} and ε are bimaterial constants which are given in terms of the compliances S_{ij} of the orthotropic layers adjacent to the crack as well as in terms of Suo's constants λ and ρ as follows

$$\begin{aligned}
H_{11} &= \left[2n\lambda^{1/4}\sqrt{S_{11}S_{22}}\right]_1 + \left[2n\lambda^{1/4}\sqrt{S_{11}S_{22}}\right]_2,\\
H_{22} &= \left[2n\lambda^{1/4}\sqrt{S_{11}S_{22}}\right]_1 + \left[2n\lambda^{1/4}\sqrt{S_{11}S_{22}}\right]_2.
\end{aligned}$$

In the above expressions the subscripts 1 and 2 were used to denote materials 1 and 2, respectively, consistent with Figure 1 and $n = \left[\frac{1}{2}(1+\rho)\right]^{1/2}$.

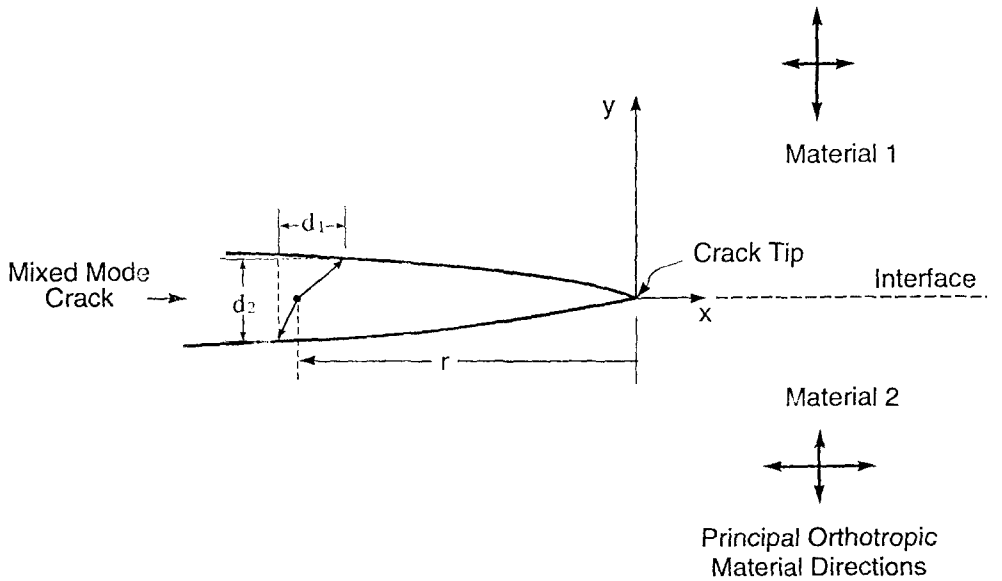

Figure 2. The near-tip crack displacement vector used in the development of the Crack Surface Displacement (CSD) method which can be used to extract the stress intensities from a known finite element solution.

In addition, the oscillatory index ε is given by

$$\varepsilon = \frac{1}{2\pi} \log \frac{1-\beta}{1+\beta},$$

where β represents a generalization of one of Dundur's parameters [9]. The displacement jump across the crack surfaces (see Figure 2) is given by

$$\sqrt{\frac{H_{11}}{H_{22}}} d_2 + i d_1 = \frac{2(2\pi)^{-(1/2)} H_{11} K^* r^{(1/2)+i\varepsilon}}{(1+2i\varepsilon)\cosh(\pi\varepsilon)}, \tag{10}$$

where $K^* = K_I^* + iK_{II}^*$ is a complex stress intensity factor and d_1 and d_2 represent crack surface separation consistent with Figure 2. As in the case of homogeneous bimaterial systems, a finite energy release rate is also obtained for the problem under consideration and it takes the form

$$\mathcal{G} = H_{11}|K^*|^2/(4\cosh^2(\pi\varepsilon)), \tag{11}$$

where $|K^*|$ represents the modulus of the complex stress intensity factor and H_{11} and ε are those defined earlier in this section. It will be shown later in this work, that (10) and (11) form the basis for the development of the CSD method in extracting stress intensities from a known finite element solution. In order to develop the energy method, however, the full near-tip displacement field is required as the auxiliary virtual displacement field consistent with the work of [1]. Thus, the expressions for the displacement and stress fields dominating the near-tip domain of an interface crack bounded by two orthotropic elastic media shall be derived next.

The general expressions for $f_1(Z_1)$ and $f_2(Z_2)$ are obtained by following Suo's work, i.e.,

$$f_1(Z_1) = \frac{1}{2(\mu_1 - \mu_2)}$$

$$\left[-\sqrt{\frac{H_{11}}{H_{22}}}\mu_2(D_1(Z_1)+D_2(Z_1))+i(D_1(Z_1)-D_2(Z_1))\right],$$

$$f_2(Z_2) = \frac{1}{2(\mu_1-\mu_2)}$$

$$\left[-\sqrt{\frac{H_{11}}{H_{22}}}\mu_2(D_1(Z_2)+D_2(Z_2))+i(D_1(Z_2)-D_2(Z_2))\right], \tag{12}$$

where D_1 and D_2 are functions of $Z_i (i = 1, 2)$ such that, when a dummy variable Z is used instead of Z_1 and Z_2, $D_1(Z)$ and $D_2(Z)$ take the forms

$$\begin{aligned} D_1(Z) &= 2\mathrm{Re}^{\pm\pi\varepsilon}K^*(1-2\varepsilon i)Z^{(1/2)+i\varepsilon}, \\ D_2(Z) &= 2\mathrm{Re}^{\mp\pi\varepsilon}\overline{K^*}(1-2\varepsilon i)Z^{(1/2)+i\varepsilon}, \end{aligned} \tag{13}$$

where $R = \frac{1}{2\sqrt{2\pi}\cosh\pi\varepsilon}\frac{1}{1+4\varepsilon^2}$ and $\overline{K^*}$ is the conjugate of K^*.

Substituting the functions f_1 and f_2 into (8), full solutions for both the near-tip displacement and stress fields can be obtained. For the purpose of this study, the virtual displacement increments, Δu_i^{I} and Δu_i^{II}, $i = 1, 2(x, y)$, due to the independent application of stress intensity increments ΔK_{I}^* and ΔK_{II}^* were found to take the following forms
when $1 < \rho < \infty$

$$\begin{aligned} \Delta u_x^{\mathrm{I}} &= \frac{R\lambda^{1/4}}{2m}\Delta K_{\mathrm{I}}^*\{[\sqrt{r}(F_1+F_2)]_{\mu_1}+[\sqrt{r}(F_3+F_4)]_{\mu_2}\}, \\ \Delta u_y^{\mathrm{I}} &= \frac{R\lambda^{1/4}}{2m}\Delta K_{\mathrm{I}}^*\{[\sqrt{r}(F_1'-F_2')]_{\mu_1}+[\sqrt{r}(F_3'-F_4')]_{\mu_2}\}, \\ \Delta u_x^{\mathrm{II}} &= -\frac{R\lambda^{1/4}}{2m}\Delta K_{\mathrm{II}}^*\{[\sqrt{r}(F_1'+F_2')]_{\mu_1}+[\sqrt{r}(F_3'+F_4')]_{\mu_2}\}, \\ \Delta u_y^{\mathrm{II}} &= \frac{R\lambda^{1/4}}{2m}\Delta K_{\mathrm{II}}^*\{[\sqrt{r}(F_1-F_2)]_{\mu_1}+[\sqrt{r}(F_3-F_4)]_{\mu_2}\}, \end{aligned} \tag{14}$$

when $-1 < \rho < 1$

$$\begin{aligned} \Delta u_x^{\mathrm{I}} &= \frac{R\lambda^{1/4}}{2m}\Delta K_{\mathrm{I}}^*\{[\sqrt{r}(F_1+F_2-F_3'+F_4')]_{\mu_1} \\ &\quad +[\sqrt{r}(F_1+F_2+F_3'-F_4')]_{\mu_2}\}, \\ \Delta u_y^{\mathrm{I}} &= \frac{R\lambda^{1/4}}{2m}\Delta K_{\mathrm{I}}^*\{[\sqrt{r}(F_1'-F_2'+F_3+F_4)]_{\mu_1} \\ &\quad +[\sqrt{r}(F_1'-F_2'-F_3-F_4)]_{\mu_2}\}, \\ \Delta u_x^{\mathrm{II}} &= -\frac{R\lambda^{1/4}}{2m}\Delta K_{\mathrm{II}}^*\{[\sqrt{r}(-F_1'-F_2'-F_3+F_4)]_{\mu_1} \\ &\quad +[\sqrt{r}(-F_1'-F_2'+F_3-F_4)]_{\mu_2}\}, \end{aligned}$$

$$\Delta u_y^{\mathrm{II}} = \frac{R\lambda^{1/4}}{2m}\Delta K_{\mathrm{II}}^{*}\{[\sqrt{r}(F_1 - F_2 - F_3' - F_4')]_{\mu_1} + [\sqrt{r}(F_1 - F_2 + F_3' + F_4')]_{\mu_2}\}. \tag{15}$$

In the above expressions, the indices μ_1 or μ_2 were used to denote that the r, F_i and F_i' terms in the corresponding brackets are evaluated consistent with the arguments of the complex numbers $Z_1 = x + \mu_1 y = \mathrm{re}^{i\phi}$ and $Z_2 = x + \mu_2 y = \mathrm{re}^{i\phi}$, respectively. In addition, the terms for F_i and F_i' are given by

$$F_i = \beta_1\gamma_i \cos\tfrac{1}{2}\phi - \beta_2\gamma_i' \sin\tfrac{1}{2}\phi,$$
$$F_i' = \beta_2\gamma_i \cos\tfrac{1}{2}\phi + \beta_2\gamma_i' \sin\tfrac{1}{2}\phi,$$

where

$$\beta_1 = \cos(\varepsilon \log r) + 2\varepsilon \sin(\varepsilon \log r),$$
$$\beta_2 = \sin(\varepsilon \log r) - 2\varepsilon \cos(\varepsilon \log r),$$

and

$$\gamma_i = Q_i\delta_j + \frac{Q_i'}{\delta_j},$$

$$\gamma_i' = Q_i\delta_j - \frac{Q_i'}{\delta_j},$$

$$\delta_j = e^{\pm(\pi-\phi)\varepsilon},$$

where j denotes material 1 or 2 and $Q_i (i = 1, 2)$ in the equation described in Appendix A.

2. Stress intensities in orthotropic bimaterial fracture

The numerical methods developed elsewhere [1] for isotropic bimaterials based on the virtual crack extension shall be extended to study the near-tip fracture characteristics associated with an interface crack embedded in orthotropic bimaterial systems. Thus, the implementation of the energy method as well as the CSD method for orthotropic systems will be presented below.

2.1. The energy method

For linear elastic systems it can be shown that the elastic energy release rate $\mathcal{G}$ associated with the near-tip stress and deformation fields is also given in terms of the J contour integral, such that $J = \mathcal{G}$. The J-integral [20] is defined as

$$J = \int_{\Gamma} W \, \mathrm{d}x_2 - n_i\sigma_{ij}\frac{\partial u_j}{\partial x_1}\,\mathrm{d}s, \tag{16}$$

where Γ represents any arbitrary open contour from the bottom crack surface around the tip to the top surface as shown in Figure 1. In (16), n is the outward unit normal to the contour, W is the strain energy density, u is the displacement vector and $\mathrm{d}s$ is an infinitesimal element of contour arc length. For elastic systems whose mechanical response is associated with an

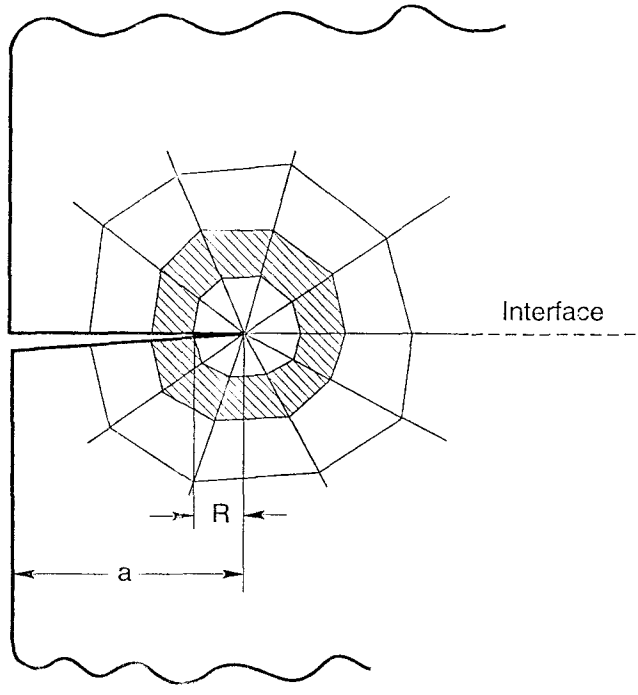

Figure 3. The shaded ring of elements is distorted during the J-integral evaluation. The finite elements outside the distorted ring are frozen while those in the interior domain are translated parallel to the crack plane by an amount equal to the virtual crack extension.

elastic strain energy potential, it has been proved that the J-integral is path independent when the crack is straight, with traction free surfaces and when any material interface is parallel to the crack, such that material properties do not depend on x, i.e., the coordinate aligned with the crack plane.

The finite element method can be used to evaluate the energy release rate, J, using Park's [3, 21–22] stiffness derivative method such that

$$J = -(\partial U/\partial a)_F \approx -\tfrac{1}{2}\{u_n\}^T(\partial[S]/\partial a)\{u_n\}, \tag{17}$$

where U is the total potential energy of the body and its differentiation with respect to crack length a is carried out at fixed load, $\{u_n\}$ is a vector of displacements at finite element nodes and $[S]$ is the stiffness matrix for the mesh of elements used to solve the crack problem.

In the actual calculation, $\{u_n\}$ can be obtained by solving a crack boundary value problem through the finite element method whereas the change of the stiffness matrix caused by a small virtual crack extension, $\partial[S]/\partial a$, is evaluated by 'squeezing' a ring of elements as shown in Figure 3, and discussed elsewhere by Parks [3]. During this process, all elements outside the distorted ring are held rigid after a virtual crack extension takes place by rigidly displacing the inner core of elements. Thus, only one ring, such as the shaded one shown in Figure 3, will be distorted, contributing to the reciprocal stiffness change in (17).

Like Matos et al., [1] in developing the energy method let us consider two displacement fields u^A and u^B representing 2 solutions to two different loading boundary value problems for the crack geometry, and let the values of J associated with them be J_A and J_B. When

the displacement fields are added to give $u^C = u^A + u^B$ resulting from the simultaneous application of loadings A and B, the value of J is given by [1, 3].

$$J_C = J_A + J_B + M_1, \tag{18}$$

where M_1 is a path independent integral given by

$$M_1 = \int_\Gamma \sigma_{ij}^A \epsilon_{ij}^B \, \mathrm{d}x_2 - \left(n_i \sigma_{ij}^B \frac{\partial u_j^A}{\partial x_1} + n_i \sigma_{ij}^A \frac{\partial u_j^B}{\partial x_1} \right) \mathrm{d}s, \tag{19}$$

which can also be represented in terms of K_I^* and K_II^*, i.e.,

$$M_1 = \frac{2}{H}(K_{\mathrm{I}A}^* K_{\mathrm{I}B}^* + K_{\mathrm{II}A}^* K_{\mathrm{II}B}^*), \tag{20}$$

where $K^* = K_\mathrm{I}^* + iK_\mathrm{II}^*$ is the complex stress intensity factor to be calculated using the existing finite element solution. In light of the above background material, the energy method developed in [1] will be expanded as follows.

Let loading case A represent the actual loading applied to the finite geometry containing the bicrystal crack. The objective is to use a known finite element solution, say u^A in conjunction with the energy method, to determine the near-tip mixed mode stress intensities K_I^* and K_II^*.

As discussed in [1], the method employs the near-tip auxiliary virtual displacement fields Δu^I and Δu^II caused by virtual stress intensity increments $\Delta K^*)_\mathrm{I} = \Delta K_\mathrm{I}^* + i0$ and $\Delta K^*)_\mathrm{II} = 0 + i\Delta K_\mathrm{I}^*$, respectively. For the orthotropic bimaterial crack, the first auxiliary displacement field employed is taken to be the one derived in Section 2 of this paper corresponding to $\Delta K_\mathrm{I}^* \neq 0$ while $\Delta K_\mathrm{II}^* = 0$. When superimposing Δu^I onto the original displacement u, an increment in the J integral $\Delta_\mathrm{I} J$ is obtained using (18). More specifically, if J corresponds to the original solution u, the coupled fields $u + \Delta u^\mathrm{I}$ would yield a new value $J_\mathrm{I} = J + \Delta_\mathrm{I} J$, where

$$\Delta_\mathrm{I} J = \frac{1}{H}(\Delta K_\mathrm{I}^{*2} + 2K_\mathrm{I}^* \Delta K_\mathrm{I}^*). \tag{21}$$

Then the mode I component of the stress intensity factor K_I^* dominating the near-tip orthotropic elastic fields is given by

$$K_\mathrm{I}^* = \tfrac{1}{2} H \frac{\Delta_\mathrm{I} J}{\Delta K_\mathrm{I}^*} - \tfrac{1}{2} \Delta K_\mathrm{I}^*. \tag{22}$$

Thus, knowing the original near-tip finite element displacement field u, K_I^* is calculated through two sequential J-integral evaluations. The first J-integral evaluation is carried out with the aid of (17) and involves the original displacement u. The second evaluation is also performed using (17) with the exception that now the displacements used are the original plus the virtual auxiliary displacements Δu^I due to $\Delta K_\mathrm{I}^* \neq 0$ and $\Delta K_\mathrm{II}^* = 0$. Thus knowing ΔK_I^*, $\Delta_\mathrm{I} J$ is calculated as the difference of the two J-integrals evaluated above and thus K_I^* can be calculated using (22).

In a similar manner the mode II component of the stress intensity factor K_II^* can be calculated using the same procedure used in calculating K_I^*, but, using auxiliary virtual fields

corresponding to $\Delta K_{\mathrm{I}}^{*} = 0$ while $\Delta K_{\mathrm{II}}^{*} \neq 0$. This again would yield a J-integral increment $\Delta_{\mathrm{II}} J = J(u + \Delta^{\mathrm{II}}) - J(u)$ which can be used to calculate K_{II}^{*} as follows

$$K_{\mathrm{II}}^{*} = \tfrac{1}{2} H \frac{\Delta_{\mathrm{II}} J}{\Delta K_{\mathrm{II}}^{*}} - \tfrac{1}{2} \Delta K_{\mathrm{II}}^{*}. \tag{23}$$

Once the J-integral corresponding to the actual boundary value problem is calculated, the above energy based method involves minimal additional computations. This is due to the fact that the already computed stiffness changes $\partial[S]/\partial a$ can be used for the two additional J-evaluations required. In addition, the computational efficiency of the method is further enhanced by using only a single ring of elements in the J-integral evaluation instead of using the entire mesh. The efficiency and accuracy of the above method shall be explored using model bimaterial orthotropic geometries later on in this paper. For comparison purposes, a crack surface displacement based complementary technique in evaluating K_{I}^{*} and K_{II}^{*} will be presented next.

2.2. Crack Surface Displacement (CSD) method

This method, unlike the method presented earlier, is only partially based on energy estimates. More specifically, as a part of this method the modulus of the stress intensity factor $|K^{*}|$ is computed in terms of the energy release rate $\mathcal{G}$, via the generalized Irwin's relationship, whereas the phase angle Ψ, is obtained using the crack surface displacements predicted via the method of finite elements. As shown by [1] it is expected that the results obtained using the CSD method should be in good agreement with those predicted via the energy method, especially if sufficiently refined finite element meshes are used. An outline of the crack surface displacement method (CSD) will be briefly reviewed below and its comparison with the energy method will be presented in the next section.

As discussed earlier in this paper, the displacement jump across the crack surface is given by (10). In (10), r is the distance from the crack tip and d_1 and d_2 denote the relative displacements of two initially neighboring points on the crack surfaces behind the tip in the x and y directions, respectively, as shown in Figure 2. In developing the CSD method, let

$$\sqrt{\frac{H_{11}}{H_{22}}}\, d_2 + i d_1 = \|\Delta u\|\, \mathrm{e}^{i\varphi}, \tag{24}$$

where $\|\Delta u\|$ and φ are the modulus and phase angle of the net crack surface displacement vector, i.e., $\|\Delta u\| = \sqrt{\frac{H_{11}}{H_{22}} d_2^2 + d_1^2}, \varphi = \arctan(d_1/(\sqrt{H_{11}/H_{22}}\, d_2))$. The complex stress intensity factor is given either in terms of its components K_{I}^{*} and K_{II}^{*} or its modulus $|K^{*}|$ and phase angle Ψ such that $K^{*} = K_{\mathrm{I}}^{*} + i K_{\mathrm{II}}^{*} = |K^{*}|\, \mathrm{e}^{i\Psi}$. In light of the above, (10) can be rewritten as follows

$$\|\Delta u\|\, \mathrm{e}^{i\phi} = \alpha \sqrt{r} |K^{*}|\, \mathrm{e}^{i(\Psi + \varepsilon \log(r/h) - \omega)}, \tag{25}$$

where

$$\alpha = \frac{1}{\sqrt{2\pi}} \frac{2H_{11}}{\sqrt{1 + 4\varepsilon^4} \cosh(\pi\varepsilon)},$$

and

$$\omega = \arctan(2\varepsilon).$$

From the above equation we finally obtain

$$\Psi = \varphi - \varepsilon \log(r/h) + \omega. \tag{26}$$

It is clear that with the use of (25) the finite displacements along the crack surface, i.e., Δu_1 and Δu_2 can be used to obtain an estimate of both the phase angle Ψ and the modulus $|K^*|$. However, the modulus $|K^*|$ can also be evaluated independently using the J-integral calculated via (11), i.e.,

$$|K^*| = \left[\frac{J}{H_{11}}\right]^{1/2} 2\cosh(\pi\varepsilon). \tag{27}$$

Such dual $|K^*|$ estimates will be used in the CSD method as an internal consistency check, identifying the finite element nodes for optimal phase angle Ψ estimates.

3. Numerical results and comparison of methods

The energy and CSD methods presented above were implemented into an integrated finite element code capable of handling generally orthotropic materials. The integrated scheme includes a pre-processor for mesh generation, the finite element processor and the fracture mechanics post-processor incorporating the energy and CSD codes. The testing and comparison of the two methods will be carried out with the aid of two model specimen geometries. These geometries are shown in Figures 4 and 5. Initially, the four-point bending pre-notched delamination specimen shown in Figure 4 will be studied. This specimen also known as the UCSB specimen was first analyzed by Charalambides et al. [23] for isotropic bimaterials. In this work the layers will be allowed an arbitrary degree of orthotropy as measured through Suo's constants λ and ρ. Thus, finite element calculations will be carried out with the aid of the integrated numerical scheme and results regarding the delamination energy release rate $\mathcal{G}$ and its associated phase angle Ψ will be sought via the use of the fracture mechanics post-processor, thus enabling the testing and comparison of the energy and CSD methods. Similar calculations will be carried out using the same specimen morphology as in the first case subjected to remote axial loads as shown in Figure 5. The finite element predictions will be compared to available analytical solutions for orthotropic materials. These calculations will be used to establish the validity of the energy and CSD methods for a wider class of applied loadings associated with mixed mode fracture of orthogonal bimaterials.

3.1. Four-point bending specimen

The numerical finite element analysis is carried out using the symmetric half of the specimen shown in Figure 4. The finite element model used in the analysis is shown in Figure 6. The model contains a total of 464 eight-noded isoparametric elements. The integrated program also allows for the use of four-noded isoparametric elements. However, in this study, and for comparison purposes with results obtained elsewhere by Charalambides [8], we will be using the eight-noded elements exclusively. As shown in Figures 6(a) and 6(b), special attention

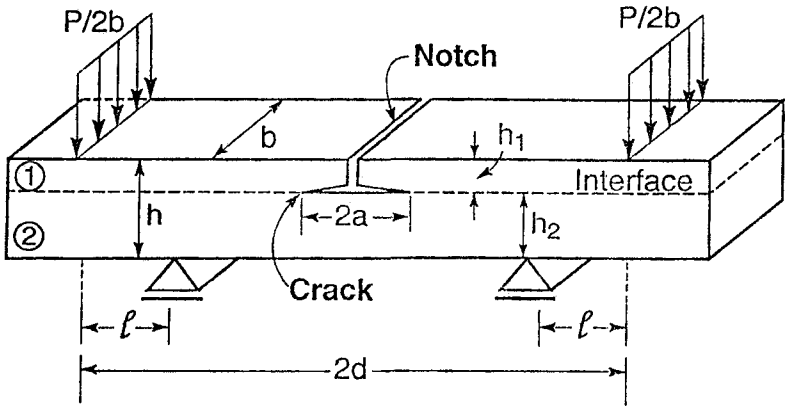

Figure 4. The pre-notched, four-point bending delamination specimen.

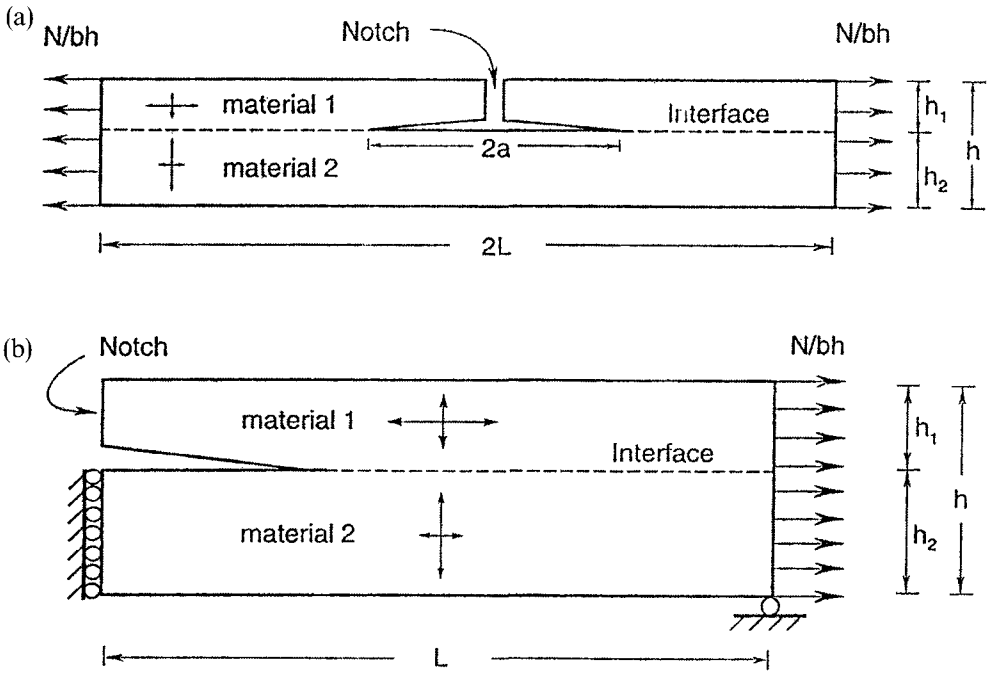

Figure 5. (a) The pre-notched, tension delamination specimen; (b) The symmetric half used in the finite element studies.

was given in discretizing the near-tip region. As discussed by Charalambides et al. [23, 24], a focused mesh was employed in order to approximate best the near-tip high gradient elastic fields. Quarter point singularity elements were used for all elements adjacent to the crack tip. Displacement and traction boundary conditions were used to simulate the symmetric four-point bending loading environment. Finally, the calculations involved orthotropic material strips under plane strain conditions.

For the purpose of comparing the numerical results to analytical solutions, the steady-state energy release rate $\mathcal{G}_{ss}$ obtained in a manner described elsewhere [8], will be used. Without loss of generality, the comparison between the numerical and analytically predicted energy

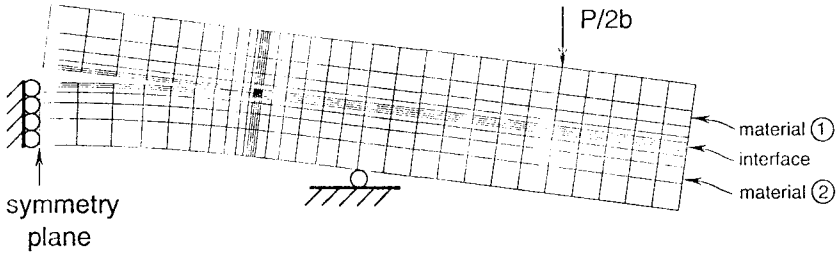

(a)

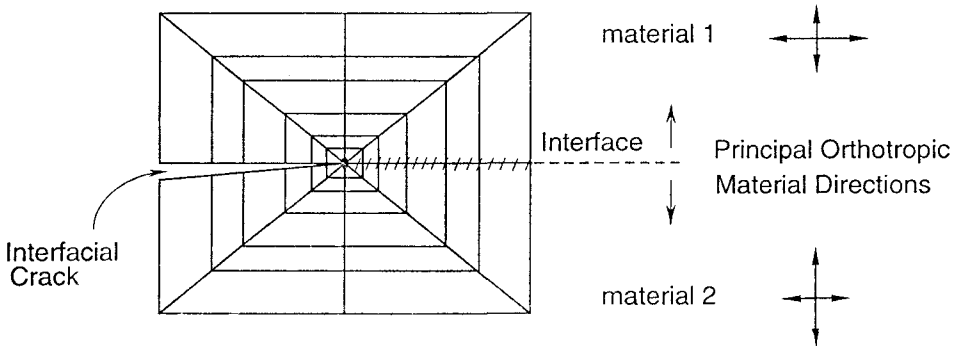

(b)

Figure 6. Four-point bending model and the mesh used in the finite element calculations. (a) The deformed body; (b) The deformed crack tip region.

release rates will be performed assuming that both material strips are made out of the same orthotropic material, and that they are of equal thickness, i.e., $\rho_1 = \rho_2, \lambda_1 = \lambda_2$ and $h_1 = h_2$. Here, λ and ρ are the Suo's parameters for each material strip and the subscripts 1 and 2 are used to represent materials 1 and 2, respectively. Under these conditions, the analytical steady-state energy release rate normalized by $E_1(1+\zeta)I/(1-\nu_{12}\nu_{21})M_0^2$, i.e., $\hat{\mathcal{G}}_{ss}$, is given by

$$\hat{\mathcal{G}}_{ss} = \tfrac{7}{2}(1+\zeta), \tag{28}$$

where $\zeta = \lambda_1/\lambda_2$.

The aim of the results presented below is to establish the validity, efficiency and effectiveness of the energy of CSD methods for mixed mode interface bicrystal fracture calculations. The results will be presented both in a tabulated form and when appropriate they will be presented graphically in 2-dimensional plots.

The sensitivity of the energy and CSD methods to material dissimilarity in bimaterial orthotropic fracture is further explored with the aid of the four-point bending delamination model shown in Figure 6. As discussed earlier, this model contains 464 eight-noded isoparametric elements with a near-tip focused mesh designed to capture high stress gradients. The total number of elements was chosen consistent with the mesh sensitivity results presented in

Table 1. Steady-state energy release rates obtained analytically via (28) and numerically using the energy method for various λ and ρ orthotropic constants. These results were obtained for $\rho_1 = \rho_2 = \rho, \lambda_1 = \lambda_2 = \lambda$ and $h_1 = h_2$. The energy release rates were normalized by $E_1(1+\zeta)I/(1-\nu_{12}\nu_{21})M_0^2$

λ	ρ	$\widehat{\mathcal{G}}_{ss}$ Analytical (27)	$\widehat{\mathcal{G}}_{ss}$ Energy Method	% Error
1.000	0.0476	7.0	6.9006	1.42
0.500	0.1045	7.0	6.9967	0.05
0.250	0.1740	7.0	7.1007	1.44
0.167	0.2238	7.0	7.1188	1.70
0.125	0.2646	7.0	7.1124	1.61
0.100	0.3000	7.0	7.0962	1.37

Table 2. Trends in the normalized energy release rate $\widehat{\mathcal{G}}$ and normalized stress intensity factor components $\widehat{K}_{\mathrm{I}}^{*}$ and $\widehat{K}_{\mathrm{II}}^{*}$ with normalized crack length a/l for a homogeneous system comprised of layers of equal thickness, i.e., $h_1 = h_2$. Columns marked by 1 and 2 correspond to results obtained by the energy and CSD methods, respectively. The energy release rates were normalized by $E_1(1+\zeta)I/(1-\nu_{12}\nu_{21})M_0^2$ and the stress intensities were normalized by $bh^{3/2}/Pl$. The results were obtained using the four-point bending delamination specimen shown in Figure 4

$\zeta = \frac{\lambda_1}{\lambda_2}$	$\frac{\rho_1}{\rho_2}$	a/l	$\widehat{\mathcal{G}}$	$\widehat{K}_{\mathrm{I}}^{*}$ (1)	$\widehat{K}_{\mathrm{I}}^{*}$ (2)	$\widehat{K}_{\mathrm{II}}^{*}$ (1)	$\widehat{K}_{\mathrm{II}}^{*}$ (2)	$\Psi(1)$ degrees	$\Psi(2)$ degrees
1.0	1.0	0.1	6.9541	1.8263	1.8206	1.5223	1.5222	39.8134	39.8988
1.0	1.0	0.2	7.0612	1.8126	1.8041	1.5675	1.5695	40.8571	41.0224
1.0	1.0	0.3	7.0993	1.8132	1.8043	1.5769	1.5791	41.0127	41.1907
1.0	1.0	0.4	7.1116	1.8146	1.8055	1.5787	1.5807	41.0231	41.2024
1.0	1.0	0.5	7.1154	1.8161	1.8066	1.5785	1.5804	40.9960	41.1798
1.0	1.0	0.6	7.1224	1.8181	1.8083	1.5785	1.5801	40.9636	41.1472
1.0	1.0	0.7	7.1299	1.8207	1.8105	1.5779	1.5794	40.9138	41.0996
1.0	1.0	0.8	7.1403	1.8241	1.8135	1.5774	1.5786	40.8519	41.0382
1.0	1.0	0.9	7.1123	1.8277	1.8164	1.5752	1.5762	40.7571	40.9516
1.0	1.0	1.0	7.1403	1.8298	1.8179	1.5725	1.5732	40.6741	40.8727
1.0	1.0	1.2	6.9726	1.8029	1.7903	1.5623	1.5612	40.9106	41.0882
1.0	1.0	1.5	4.4747	1.0590	1.2820	1.4177	1.4048	47.6679	47.6171
Inner Loading Point; $a/l = 1.5$									
1.0	1.0	1.8	1.4639	0.6327	0.6172	0.9140	0.8922	55.3055	55.3241
1.0	1.0	2.0	0.4746	0.2778	0.2615	0.5968	0.5539	65.0404	64.7322
Outer Loading Point; $a/l = 2.5$									

Table 3. Trends in the normalized energy release rate $\widehat{\mathcal{G}}$ and normalized stress intensity factor components $\widehat{K}_{\mathrm{I}}^{*}$ and $\widehat{K}_{\mathrm{II}}^{*}$ with normalized crack length a/l for an orthogonal bimaterial system wherein $\lambda_1/\lambda_2 = 10.0, \rho_1/\rho_2 = 3.162$ and normalized notch depth $h_1/h_2 = 1.0$. Columns marked by 1 and 2 correspond to results obtained by the energy and CSD methods, respectively. The energy results were normalized by $E_1(1+\zeta)\mathrm{I}(1-\nu_{12}\nu_{21})M_0^2$ and the stress intensities were normalized by $bh^{3/2}/Pl$. The results were obtained using the four-point bending delamination specimen shown in Figure 4

$\zeta = \frac{\lambda_1}{\lambda_2}$	$\frac{\rho_1}{\rho_2}$	a/l	$\widehat{\mathcal{G}}$	$\widehat{K}_{\mathrm{I}}^{*}$ (1)	$\widehat{K}_{\mathrm{I}}^{*}$ (2)	$\widehat{K}_{\mathrm{II}}^{*}$ (1)	$\widehat{K}_{\mathrm{II}}^{*}$ (2)	$\Psi(1)$ degrees	$\Psi(2)$ degrees
10.0	3.162	0.1	41.0758	1.5012	1.5079	2.0103	1.9918	53.2485	52.8734
10.0	3.162	0.2	40.9611	1.4622	1.4657	2.0328	2.0186	54.0166	53.7259
10.0	3.162	0.3	41.0738	1.4567	1.4619	2.0384	2.0253	54.4128	54.1775
10.0	3.162	0.4	41.0854	1.4581	1.4614	2.0383	2.0258	54.4227	54.1935
10.0	3.162	0.5	41.0449	1.4579	1.4610	2.0365	2.0242	54.4028	54.1807
10.0	3.162	0.6	41.0005	1.4577	1.4605	2.0348	2.0224	54.3818	54.1635
10.0	3.162	0.7	40.9400	1.4580	1.4603	2.0325	2.0197	54.3467	54.1332
10.0	3.162	0.8	40.8732	1.4588	1.4603	2.0301	2.0166	54.2994	54.0897
10.0	3.162	0.9	40.7718	1.4605	1.4609	2.0260	2.0117	54.2121	54.0123
10.0	3.162	1.0	40.6439	1.4628	1.4618	2.0209	2.0054	54.1001	53.9094
10.0	3.162	1.2	40.0527	1.4615	1.4575	2.0034	1.9843	53.8884	53.7019
10.0	3.162	1.5	26.3451	0.9674	0.9649	1.7829	1.7417	61.5147	51.0138
Inner Loading Point; $a/l = 1.5$									
10.0	3.162	1.8	7.4475	0.4384	0.4001	1.0644	0.9585	67.6143	67.3453
10.0	3.162	2.0	2.1365	0.1528	0.0919	0.6556	0.3670	76.8824	75.9428
Outer Loading Point; $a/l = 2.5$									

Table 4. Trends in the normalized steady-state energy release rate $\widehat{\mathcal{G}}_{ss}$ and normalized stress intensity factor components $\widehat{K}_{\mathrm{I}}^{*}$ and $\widehat{K}_{\mathrm{II}}^{*}$ with the normalized notch depth, h_1/h_2, under a material ratio $\lambda_1/\lambda_2 = 1.0$ and a normalized crack length $a/l = 1.0$. Columns marked by 1 and 2 correspond to results obtained by the energy and CSD methods, respectively. The energy results were normalized by $E_1(1+\zeta)I(1-\nu_{12}\nu_{21})M_0^2$ and the stress intensities were normalized by $bh^{3/2}/Pl$. The results were obtained using the four-point bending delamination specimen shown in Figure 4

$\zeta = \frac{\lambda_1}{\lambda_2}$	$\frac{\rho_1}{\rho_2}$	h_1/h_2	$\widehat{\mathcal{G}}_{ss}$	$\widehat{K}_{\mathrm{I}}^{*}$ (1)	$\widehat{K}_{\mathrm{I}}^{*}$ (2)	$\widehat{K}_{\mathrm{II}}^{*}$ (1)	$\widehat{K}_{\mathrm{II}}^{*}$ (2)	$\Psi(1)$ degrees	$\Psi(2)$ degrees
1.0	1.0	0.20	0.7742	0.5394	0.5419	0.5828	0.5772	47.2148	46.8072
1.0	1.0	0.25	1.0094	0.6263	0.6272	0.6555	0.6509	46.3058	46.0621
1.0	1.0	0.50	2.4676	1.0306	1.0265	0.9730	0.9717	43.3524	43.4288
1.0	1.0	1.00	7.1403	1.8298	1.8179	1.5725	1.5732	40.6741	40.8727
1.0	1.0	1.50	14.8380	2.6855	2.6657	2.2163	2.2135	39.5328	39.7058
1.0	1.0	2.00	26.2588	3.6094	3.5785	2.9153	2.9033	38.9284	39.0529

Table 5. Steady-state energy release rates obtained analytically via (29) and numerically using the energy method for various λ and ρ orthotropic constants. These results were obtained using the tension delamination specimen for $\lambda = \lambda_1 = \lambda_2$, $\rho = \rho_1 = \rho_2$ and $h_1 = h_2$. The energy release rates were normalized by $E_1(1+\zeta)I/(1-\nu_{12}\nu_{21})N^2h^2$

λ	ρ	$\widehat{\mathcal{G}}_{ss}$ Analytical (27)	$\widehat{\mathcal{G}}_{ss}$ Energy method	% Error
1.000	0.0476	0.5833	0.5709	2.13
0.500	0.1045	0.5833	0.5738	1.63
0.250	0.1740	0.5833	0.5783	0.86
0.167	0.2238	0.5833	0.5798	0.61
0.125	0.2646	0.5833	0.5808	0.43
0.100	0.3000	0.5833	0.5818	0.26

Table 6. Trends in the normalized energy release rate $\widehat{\mathcal{G}}$ and normalized stress intensity factor components $\widehat{K}^*_{\mathrm{I}}$ and $\widehat{K}^*_{\mathrm{II}}$ with normalized crack length a/l for a homogeneous system comprised of layers of equal thickness, i.e., $h_1 = h_2$. Columns marked by 1 and 2 correspond to results obtained by the energy and CSD methods respectively. The energy release rates were normalized by $E_1(1+\zeta)I/(1-\nu_{12}\nu_{21})N^2h^2$ whereas the stress intensities were normalized by $bh^{1/2}/N$. The results were obtained using the tension delamination specimen shown in Figure 5

$\zeta = \frac{\lambda_1}{\lambda_2}$	$\frac{\rho_1}{\rho_2}$	a/l	$\widehat{\mathcal{G}}$	$\widehat{K}^*_{\mathrm{I}}$ (1)	$\widehat{K}^*_{\mathrm{I}}$ (2)	$\widehat{K}^*_{\mathrm{II}}$ (1)	$\widehat{K}^*_{\mathrm{II}}$ (2)	$\Psi(1)$ degrees	$\Psi(2)$ degrees
1.0	1.0	0.1	0.6051	0.9384	0.9368	0.9855	0.9831	46.4006	46.3817
1.0	1.0	0.2	0.6155	0.9114	0.9064	1.0264	1.0266	48.3953	48.5562
1.0	1.0	0.3	0.6234	0.9057	0.8998	1.0431	1.0438	49.0324	49.2396
1.0	1.0	0.4	0.6273	0.9051	0.8988	1.0495	1.0503	49.2254	49.4458
1.0	1.0	0.5	0.6290	0.9053	0.8988	1.0519	1.0527	49.2840	49.5085
1.0	1.0	0.6	0.6296	0.9054	0.8989	1.0527	1.0536	49.3029	49.5287
1.0	1.0	0.7	0.6298	0.9054	0.8989	1.0531	1.0539	49.3101	49.5363
1.0	1.0	0.8	0.6298	0.9054	0.8989	1.0532	1.0540	49.3138	49.5402
1.0	1.0	0.9	0.6298	0.9054	0.8988	1.0532	1.0540	49.3165	49.5432
1.0	1.0	1.0	0.6297	0.9053	0.8987	1.0532	1.0539	49.3194	49.4561
1.0	1.0	1.2	0.6294	0.9051	0.8983	1.0532	1.0538	49.3269	49.5537
1.0	1.0	1.5	0.6288	0.9044	0.8974	1.0532	1.0535	49.3463	49.5735
1.0	1.0	1.8	0.6277	0.9031	0.8939	1.0530	1.0531	49.3833	49.6113
1.0	1.0	2.0	0.6265	0.9016	0.8943	1.0529	1.0528	49.4250	49.6541

Figures 7a and 7b, such that a sufficiently accurate finite element solution could be obtained. The objective of this part of the study is to establish the generality of the proposed methods with respect to the material systems involved in mixed mode fracture of orthotropic bimaterials. Initially, the special case wherein fracture occurs at the interface of two equal thickness orthotropic layers is considered. For this system, analytical predictions obtained using (28)

Table 7. Trends in the normalized energy release rate $\widehat{\mathcal{G}}$ and normalized stress intensity factor components $\widehat{K}^*_{\mathrm{I}}$ and $\widehat{K}^*_{\mathrm{II}}$ with normalized crack length a/l for an orthogonal bimaterial system wherein $\lambda_1/\lambda_2 = 10.0, \rho_1/\rho_2 = 3.162$ and normalized notch depth $h_1/h_2 = 1.0$. Columns marked by 1 and 2 correspond to results obtained by the energy and CSD methods, respectively. The energy results were normalized by $E_1(1+\zeta)I/(1-\nu_{12}\nu_{21})N^2h^2$ and the stress intensities were normalized by $bh^{1/2}/N$. The results were obtained using the tension delamination specimen shown in Figure 5

$\zeta = \frac{\lambda_1}{\lambda_2}$	$\frac{\rho_1}{\rho_2}$	a/l	$\widehat{\mathcal{G}}$	$\widehat{K}^*_{\mathrm{I}}$ (1)	$\widehat{K}^*_{\mathrm{I}}$ (2)	$\widehat{K}^*_{\mathrm{II}}$ (1)	$\widehat{K}^*_{\mathrm{II}}$ (2)	$\Psi(1)$ degrees	$\Psi(2)$ degrees
10.0	3.162	0.1	3.5134	0.7756	0.7715	1.2359	1.2310	57.8897	57.9251
10.0	3.162	0.2	3.4380	0.7175	0.7084	1.2515	1.2500	60.1726	60.4605
10.0	3.162	0.3	3.4492	0.7034	0.7004	1.2616	1.2571	60.8565	60.8737
10.0	3.162	0.4	3.4616	0.7002	0.6897	1.2659	1.2659	61.0524	61.4189
10.0	3.162	0.5	3.4676	0.6993	0.6889	1.2673	1.2677	61.1093	61.4784
10.0	3.162	0.6	3.4696	0.6990	0.6887	1.2676	1.2683	61.1277	61.4958
10.0	3.162	0.7	3.4697	0.6986	0.6886	1.2674	1.2683	61.1356	61.5018
10.0	3.162	0.8	3.4689	0.6983	0.6884	1.2670	1.2682	61.1407	61.5048
10.0	3.162	0.9	3.4676	0.6979	0.6955	1.2667	1.2639	61.1454	61.1758
10.0	3.162	1.0	3.4659	0.6975	0.6953	1.2661	1.2636	61.1503	61.1787
10.0	3.162	1.2	3.4619	0.6966	0.6946	1.2652	1.2628	61.1623	61.1862
10.0	3.162	1.5	3.4539	0.6950	0.6932	1.2636	1.2614	61.1882	61.2059
10.0	3.162	1.8	3.4425	0.6928	0.6911	1.2619	1.2594	61.2307	61.2430
10.0	3.162	2.0	3.4320	0.6908	0.6891	1.2605	1.2578	61.2746	61.2842

Table 8. Trends in the normalized steady-state energy release rate $\widehat{\mathcal{G}}_{ss}$ and normalized stress intensity factor components $\widehat{K}^*_{\mathrm{I}}$ and $\widehat{K}^*_{\mathrm{II}}$ with the normalized notch depth, h_2/h_1, under a material ratio $\lambda_1/\lambda_2 = 1.0$ and a normalized crack length $a/l = 1.0$. Columns marked by 1 and 2 correspond to results obtained by the energy and CSD methods respectively. The energy results were normalized by $E_1(1+\zeta)I(1-\nu_{12}\nu_{21})N^2h^2$ and the stress intensities were normalized by $bh^{1/2}/N$. The results were obtained using the tension delamination specimen shown in Figure 5

$\zeta = \frac{\lambda_1}{\lambda_2}$	$\frac{\rho_1}{\rho_2}$	h_1/h_2	$\widehat{\mathcal{G}}$	$\widehat{K}^*_{\mathrm{I}}$ (1)	$\widehat{K}^*_{\mathrm{I}}$ (2)	$\widehat{K}^*_{\mathrm{II}}$ (1)	$\widehat{K}^*_{\mathrm{II}}$ (2)	$\Psi(1)$ degrees	$\Psi(2)$ degrees
1.0	1.0	0.20	0.0322	0.1880	0.1883	0.2438	0.2425	52.3613	52.1660
1.0	1.0	0.25	0.0450	0.2237	0.2235	0.2888	0.2878	52.2327	52.1718
1.0	1.0	0.50	0.1480	0.4183	0.4156	0.5222	0.5222	51.3056	51.4835
1.0	1.0	1.00	0.6297	0.9053	0.8987	1.0532	1.0539	49.3194	49.5461
1.0	1.0	1.50	1.6449	1.5149	1.5048	1.6642	1.6638	47.6884	47.8724
1.0	1.0	2.00	3.3918	2.2310	2.2179	2.3450	2.3407	46.4267	46.5437

are compared to those obtained using the energy equation in conjunction with the finite element solution obtained using the model shown in Figure 6 discussed above. Comparison results obtained for various values of the orthotropic constant λ and ρ are presented in Table 1. As shown, the percentage error between the analytical and numerical results is less than 1.7

percent even when highly orthotropic layers are measured through the λ and ρ constants are considered. For the finite element model used, the CSD results were consistent with those predicted by the energy method and thus were not included in Table 1. Tables 2 and 3 contain results for the normalized energy release rate $\widehat{\mathcal{G}} = \mathcal{G}(E_1(1+\zeta)I/(1-\nu_{12}\nu_{21})M_0^2)$, and the associated stress intensities $\widehat{K_I^*} = K_I^*(bh^{3/2}/Pl)$ and $\widehat{K_{II}^*} = \widehat{K_{II}^*} = K_{II}^*(bh^{3/2}/Pl)$ obtained using the energy and CSD methods. In the normalization factor, $I = h^3/12$, $M_0 = Pl$ with P and l shown in Figure 6, E_1 is the longitudinal modulus of the top layer and ν_{12} and ν_{21} are the major Poisson's ratios of the orthotropic layer. The results reported in Tables 2 and 3 aim at exploring the potential of the energy and CSD methods by systematically varying the crack length for fixed orthogonal bimaterial systems. For example, the results shown in Table 2 were obtained for a homogeneous orthotropic system, i.e., $\lambda_1 = \lambda_2, \rho_1 = \rho_2$ and layers of equal thickness $h_1 = h_2$. These results are in excellent agreement with those reported elsewhere by Charalambides [7] for isotropic materials where in the expression for the energy release rate the normalizing modulus is now being replaced by the longitudinal modulus E_1 of the orthotropic layer. Evidently, the phase angle predictions appear to be minimally affected by the degree of orthotropy consistent with the results reported in Table 2. Table 3 and Figure 8 contain similar results for a different bimaterial system. As can be seen through these results, the energy and CSD methods give consistent predictions of the mode mixity dominating delamination over a wide range of crack lengths. Such results increase our confidence in both methods especially when finite element meshes consistent with those used in our convergence studies are used. Further comparisons of the energy and CSD methods are made using the results tabulated in Table 4, where the normalized notch depth h_1/h_2 is varied over a wide range while fixing the material systems and delamination crack length a/l.

3.2. Tension delamination specimen

In order to explore the effects of remotely applied loadings on the energy and CSD methods, the orthogonal bimaterial delamination specimen subjected to remote tension shall be analyzed next. The specimen geometry is shown in Figure 5. A finite element mesh similar to that used for the four-point bending geometry shown in Figures 6(a) and 6(b) was also used for the discretization of the geometry shown in Figure 5. As in the case of the four-point bending specimen, due to symmetry, the finite element solutions are sought for only the right half of the specimen. The general approach in analyzing this specimen is similar to that used for the four-point bending delamination geometry. Clearly, in this analysis, the boundary conditions used are those consistent with the loading and deformation characteristics governing the specimen geometry shown in Figure 5. As before, special attention was given in discretizing the crack tip region. Like the previous case, solutions for various bimaterial systems will be presented. For comparison purpose, the steady-state analytical energy release rate $\mathcal{G}_{ss}$ obtained through energy balance considerations will be developed. More specifically, for the special case whereby $\rho_1 = \rho_2, \lambda_1 = \lambda_2$ and $h_1 = h_2$, the expression for the analytical steady-state energy release rate [8] normalized by $E_1(1+\zeta)I/(1-\nu_{12}\nu_{21})N^2h^2$, i.e., $\widehat{\mathcal{G}}_{ss}$, takes the form

$$\widehat{\mathcal{G}}_{ss} = \tfrac{7}{24}(1+\zeta), \tag{29}$$

where $\zeta = \lambda_1/\lambda_2$.

Comparison between the numerical results and those predicted via (29) are shown in Table 5. It can be found that the numerical and analytical solutions are in good agreement.

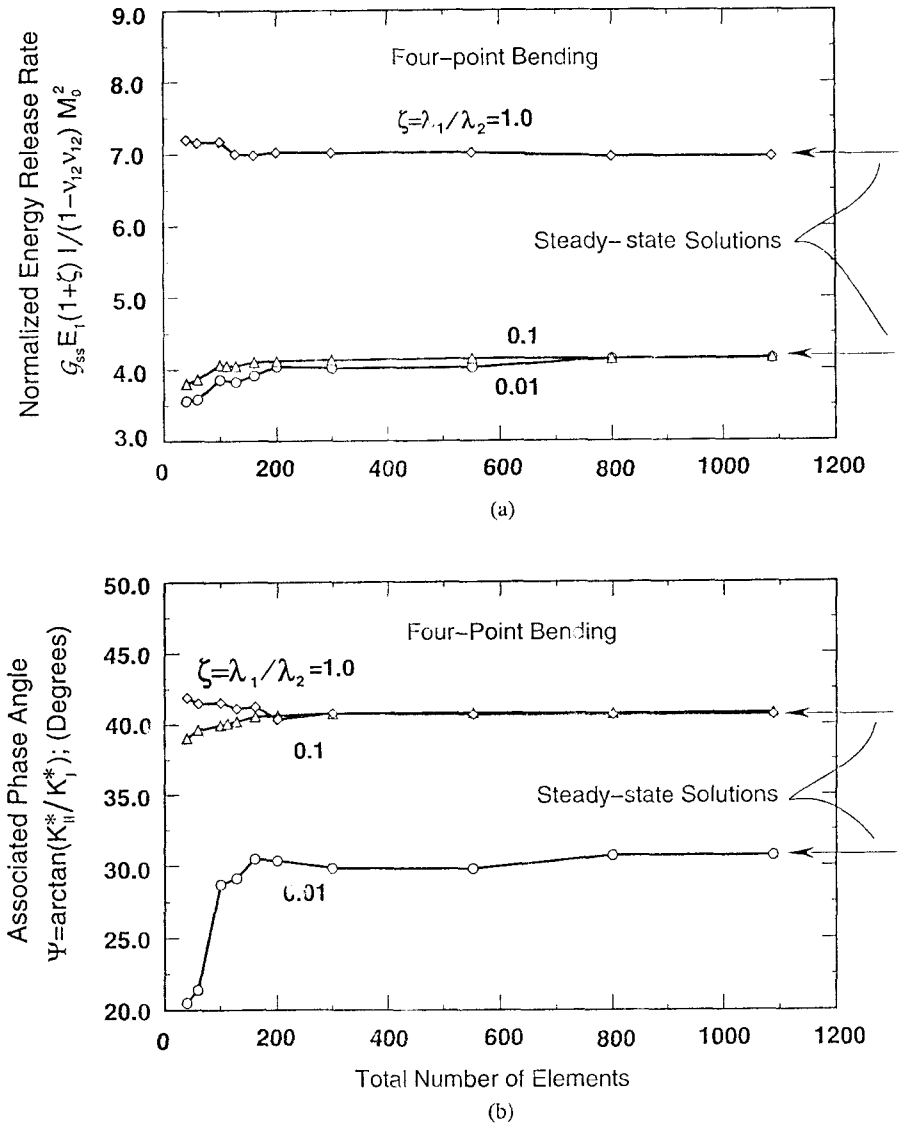

Figure 7. Mesh sensitivity studies depicting trends of the near-tip energy release rate $\mathcal{G}$ (a) and associate phase angle Ψ, (b) as a function of total number of elements used. These results were obtained using eight-noded isoparametric elements.

The deviation between the numerical and analytical results for the various bimaterial pairs is no more than 2.15 percent when 464 elements were used.

Further calculations for comparisons of the energy and CSD methods were carried out on the tension bimaterial specimen shown in Figure 5. Results similar to those discussed for the four-point bending specimen for the normalized energy release rate $\widehat{\mathcal{G}} = \mathcal{G}(E_1(1+\zeta)\mathrm{I}/(1-\nu_{12}\nu_{21})N^2h^2)$, and the associated stress intensities $\widehat{K^*}_{\mathrm{I}} = K^*_{\mathrm{I}}(bh^{1/2}/N)$ and $\widehat{K^*}_{\mathrm{II}} = K^*_{\mathrm{II}}(bh^{1/2}/N)$ obtained using two methods are presented in Tables 6 and 7 and Figure 9. In the normalization factor, $\mathrm{I} = h^3/12$, E_1 is the longitudinal modulus of the top layer, ν_{12} and ν_{21} are the major Poisson's ratios of the orthotropic layer. Further comparisons of the energy and CSD methods are made using results tabulated in Table 8, which correspond to various

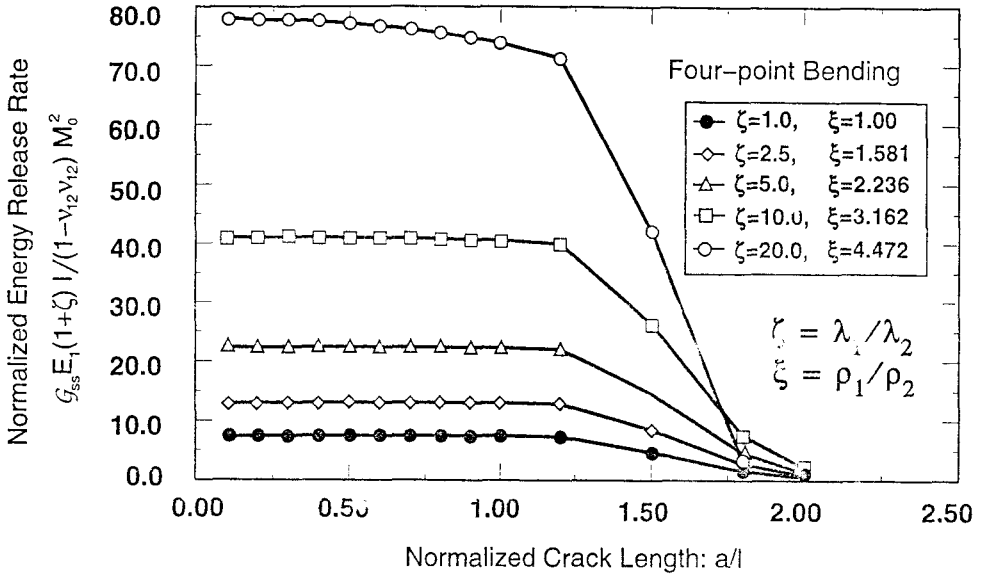

Figure 8a. Trends in the normalized energy release rate $\widehat{\mathcal{G}}$ with normalized crack length for various bimaterial pairs. These results were obtained using the four-point bending bimaterial specimen, under plane strain conditions and normalized notch depth $h_1/h_2 = 1.0$.

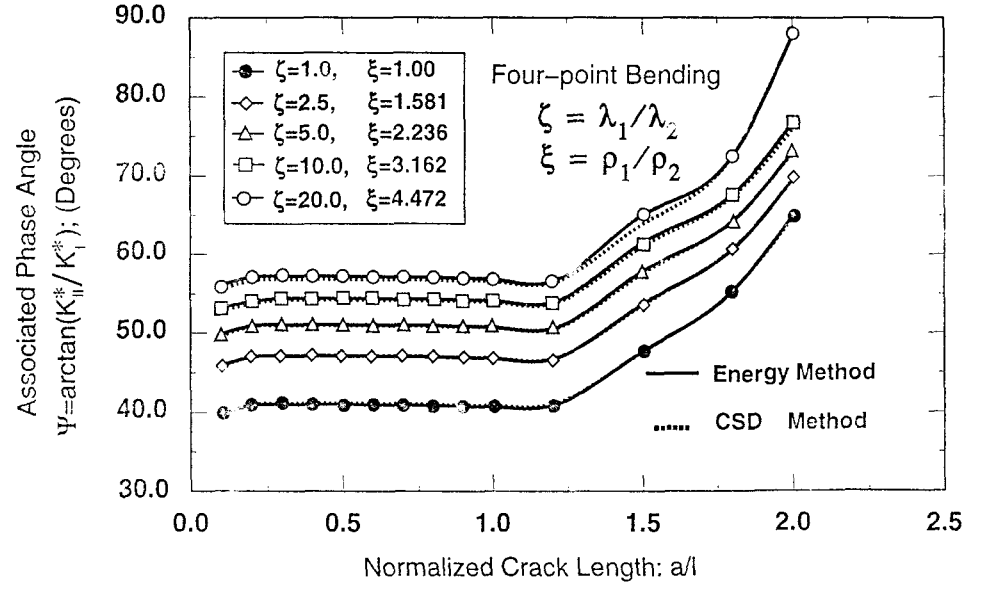

Figure 8b. Trends in the associated phase angle Ψ with normalized crack length for various bimaterial pairs. These results were obtained using the four-point bending bimaterial specimen, under plane strain conditions and normalized notch depth $h_1/h_2 = 1.0$.

normalized notch depth ratios: h_1/h_2. As in the case of the four point bending specimen, the CSD and energy methods in the case of the tension specimen gave consistent results for a wide range of orthotropic bimaterial systems.

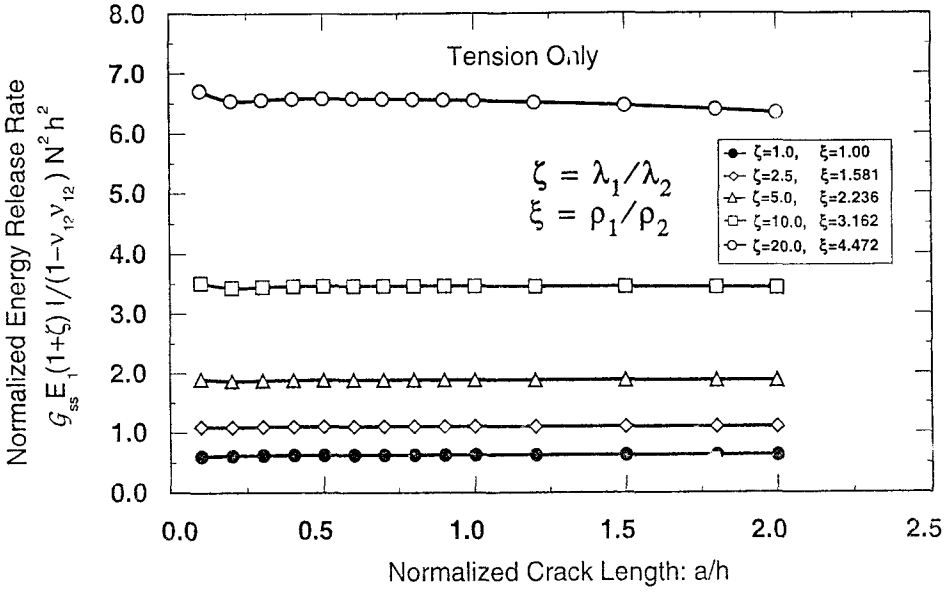

Figure 9a. Trends in the normalized energy release rate $\widehat{\mathcal{G}}$ with normalized crack length for various bimaterial pairs. These results were obtained using the tension bimaterial specimen under plane strain conditions and normalized notch depth $h_1/h_2 = 1.0$.

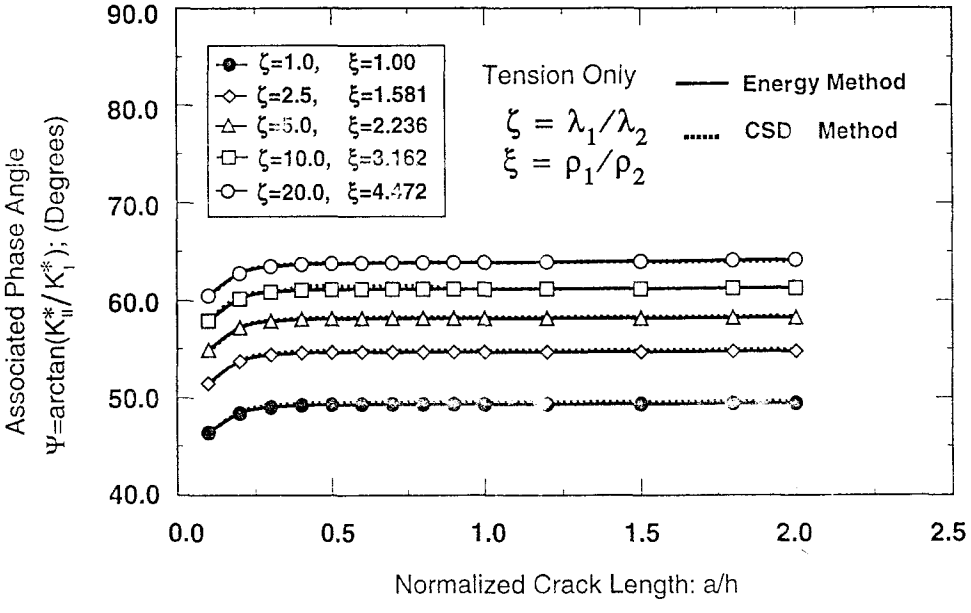

Figure 9b. Trends in the associated phase angle Ψ with normalized crack length for various bimaterial pairs. These results were obtained using the tension bimaterial specimen under plane stress condition and normalized notch depth $h_1/h_2 = 1.0$.

4. Closure

An energy and a Crack Surface Displacement (CSD) numerical method have been developed enabling fracture studies of orthotropic bimaterial interfaces. The methods presented in this work expand the scope of existing techniques used in fracture mechanics studies of isotropic

bimaterials. Both the energy and CSD methods require that a finite element solution of the orthotropic possibly laminate geometry be known. Given that such a solution exists, the energy and CSD method can be used to extract the individual stress intensities dominating the region of an interface bicrystal crack embedded within the domain of the known finite element solution.

Mesh sensitivity studies indicated that both methods give consistent, sufficiently accurate stress intensity predictions when the model contains more than 200 eight-noded isoparametric finite elements with the near-tip regime descretized using a focused mesh. The energy method however, was found to be more robust even when used with coarse meshes. The methods developed in this work provide a set of numerical tools which can be used to study mixed mode delimination phenomena often observed in brittle and resin matrix composite laminates.

5. Appendix A

In (16),

$$\begin{aligned} Q_1 &= (a_{11} - a_{21})c_1, & Q_1' &= -(a_{11} + a_{21})c_2, \\ Q_2 &= (a_{11} + a_{21})c_1, & Q_2' &= -(a_{11} - a_{21})c_2, \\ Q_3 &= (a_{22} - a_{12})c_3, & Q_3' &= +(a_{12} + a_{22})c_4, \\ Q_4 &= -(a_{12} + a_{22})c_3, & Q_4' &= +(a_{12} - a_{22})c_4, \end{aligned} \tag{A.1}$$

and

$$\begin{aligned} c_1 &= 1 - \lambda^{-1/4}(n-m)\sqrt{\frac{H_{11}}{H_{22}}}, & c_2 &= 1 + \lambda^{-1/4}(n-m)\sqrt{\frac{H_{11}}{H_{22}}}, \\ a_{11} &= S_{12} - S_{11}\lambda^{-1/2}(n+m), & a_{12} &= S_{12} - S_{11}\lambda^{3/2}(n-m)^2, \\ a_{21} &= S_{21}\lambda^{-1/4}(n+m) - S_{22}\lambda^{1/4}(n+m)^{-1}, \\ a_{22} &= S_{21}\lambda^{-1/4}(n-m) - S_{22}\lambda^{1/4}(n-m)^{-1}, \end{aligned} \tag{A.2}$$

in (17),

$$\begin{aligned} Q_1 &= E_1 - E_7, & Q_1' &= E_2 + E_8, \\ Q_2 &= E_1 + E_7, & Q_2' &= E_2 - E_8, \\ Q_3 &= E_3 + E_5, & Q_3' &= E_6 + E_4, \\ Q_4 &= E_5 + E_3, & Q_4' &= E_4 + E_6, \end{aligned} \tag{A.3}$$

where

$$\begin{aligned} E_1 &= b_1 t_{11} - b_2 e_{11}, & E_2 &= b_1 t_{11} + b_3 e_{11}, \\ E_3 &= b_1 e_{11} + b_2 t_{11}, & E_4 &= b_1 e_{11} - b_3 t_{11}, \\ E_5 &= b_1 t_{21} - b_2 e_{21}, & E_6 &= b_1 t_{21} + b_3 e_{21}, \\ E_7 &= b_2 t_{21} + b_1 e_{21}, & E_8 &= b_1 e_{21} - b_3 t_{21} \end{aligned} \tag{A.4}$$

and

$$b_1 = m\sqrt{\frac{H_{11}}{H_{22}}}\lambda^{-(1/4)}, \qquad b_2 = 1 - n\sqrt{\frac{H_{11}}{H_{22}}}\lambda^{-(1/4)},$$

$$b_3 = 1 + n\sqrt{\frac{H_{11}}{H_{22}}}\lambda^{-(1/4)},$$

$$t_{11} = S_{12} - S_{11}\rho\lambda^{-(1/2)}, \qquad t_{21} = m\lambda^{-(1/4)}(S_{21} + \sqrt{S_{11}S_{22}}),$$

$$e_{11} = 2mnS_{11}\lambda^{-(1/2)}, \qquad e_{21} = n\lambda^{-(1/4)}(S_{21} - \sqrt{S_{11}S_{22}}). \tag{A.5}$$

Acknowledgements

This work was partially completed at Michigan Technology University. Support was provided by the National Science Foundation through a Presidential Young Investigator Award, Grant No. MSS-9157090, or CMS-9496209.

References

1. P.P.L. Matos, R.M. McMeeking, P.G. Charalambides and M.D. Drory, *International Journal of Fracture* 40 (1989) 235–254.
2. S.S. Wang and J.F. Yau, *AIAA Journal* 19 (1981) 1350–1356.
3. D.M. Parks, *International Journal of Fracture* 10 (1978) 487–502.
4. G.R. Irwin, *Journal of Applied Mechanics* 24 (1957) 361–364.
5. M.L. Williams, *Bulletin of the Seismological Society of America* 49 (1959) 199–204.
6. Z. Suo, *Proceedings, Royal Society of London A.* 427 (1990) 331–358.
7. Z. Suo, *Journal of Applied Mechanics* 57 (1990) 627–634.
8. P.G. Charalambides, *Journal of American Ceramic Society* 74 [12] (1991) 3066–3080.
9. J. Dundurs, *Journal of Applied Mechanics* 36 (1968) 650–652.
10. J.R. Rice, *Journal of Applied Mechanics* 55 (1988) 98–103.
11. J.W. Hutchinson, *Scripta Metallurgica* (1990).
12. J. Qu and J.L. Bassani, *Journal of Mechanics and Physics of Solids* 37 (1989) 417–433.
13. S.G. Lekhnitskii, *Theory of Elasticity of an Anisotropic Body* Holden Day, San Francisco: (1963).
14. J.D. Eshelby, W.T. Read and W. Shockley, *Acta Metallurgica* 1 (1953), 251–259.
15. N.I. Muskhelishvili, *Some Basic Problems of the Mathematical Theory of Elasticity*, Groningen, Holland (1953).
16. M. Gotoh, *International Journal of Fracture* 3 (1967) 253–260.
17. A. Hoenig, *Engineering Fracture Mechanics* 16 (1982) 393–403.
18. T.C.T. Ting, *International Journal of Solids and Structures* 22 (1986) 965–983.
19. J.L. Bassani and J. Qu, *Journal of Mechanics and Physics of Solids* 37 (1989) 435–453.
20. J.R. Rice, *Journal of Applied Mechanics* 35 (1968) 379–386.
21. J.R. Rice, pp. 192–308 in *Fracture, An Advance Treatise*, Vol. 2, H. Leibowitz (ed.). Academic Press, New York (1968).
22. F.H.K. Chen and R.T. Shield, *Zeitschrift Fuer Angewandte Mathematik und Physik* 28 (1977) 1–22.
23. P.G. Charalambides et al., *Mechanics of Materials* 8 (1990) 269–283.
24. P.G. Charalambides et al., *Journal of Applied Mechanics* 56 (1989) 77–82.